Available online at www.sciencedirect.com
ScienceDirect
International Journal of Heat and Mass Transfer 51 (2008) 4415–4426
International Journal of HEAT and MASS TRANSFER
www.elsevier.com/locate/ijhmt

A computational strategy for simulating heat transfer and flow past deformable objects

Anvar Gilmanov [a], Sumanta Acharya [b,*]

[a] Center for Computations and Technology, Louisiana State University, Baton Rouge, LA 70803, United States
[b] Mechanical Engineering, Louisiana State University, Baton Rouge, LA 70803, United States

Received 21 May 2007; received in revised form 13 November 2007
Available online 7 March 2008

Abstract

Simulations of flow and heat transfer around deforming objects require the accurate resolution of the moving interface. An approach that combines the Hybrid Immersed Boundary Method (*HIBM*) for handling complex moving boundaries and the Material Point Method (*MPM*) for resolving structural stresses and the movement of the deformable body is presented here. In the *HIBM*, a fixed Eulerian, curvilinear grid is generally defined, and the variable values at grid points adjacent to a curvilinear boundary are interpolated to satisfy the boundary conditions. The *MPM* is used to solve equations of the solid structure (stresses and deflection) and communicates with the flow equations through appropriate interface-boundary conditions. As a validation of the new approach for heat transfer problems, flow and heat transfer past a rigid and deforming isothermal sphere is simulated. Predictions agree well with published results of Nusselt number for flow past a rigid sphere.

Keywords: Artificial compressibility; Dual time-stepping; Immersed boundaries; Material point method; Fluid–structure interaction; Heat transfer

1. Introduction

In many applications involving heat transfer, surfaces that deform under the action of the fluid flow are encountered. These problems which involve *fluid–structure interaction* (*FSI*) require specific treatment in the vicinity of the interface. Examples include applications in thermal sprays, injection molding, and polymer processing.

Numerical approaches for solving *FSI* problems are broadly classified as: fixed-grid (Eulerian) or moving-grid (Lagrangian or Arbitrary Lagrangian–Eulerian) methods [1]. *Fixed-grid* methods generally embody *a surface-capturing* strategy [2], and the interface has a non-zero thickness and is diffuse [1]. *Moving-grid* methods belong to the *surface-tracking* family, since with these approaches the interface is maintained to be sharp with an essentially zero thickness. Popular moving-grid methods for solving *FSI* problems are the *Lagrangian* [3] and *Arbitrary LagrangianEulerian* (*ALE*) methods [4,5]. A purely Lagrangian method was employed by Belytschko and Kennedy [6], and Donea et al. [7] to study hydro-structural interactions. However, *ALE* methods are more popular, since they use a moving-grid that follows the deforming boundaries and allows the resolution needed near the boundary [4,5,8]. However, due to the need for the mesh to conform to the body at all times, they are inherently limited to problems with moderate body deformations.

Fixed-grid approaches have been widely used due to the ease of generating a fixed-grid. Different strategies with a fixed-grid have been proposed. In the *Cut-Cell Method* [9–15] the boundary cells and fluxes adjacent to the complex interface are redefined at each step. In the *Volume of Fluid Method* (*VOF*) [16,17] the interface is reconstructed from the fractional volume of fluid content in each cell through special surface functions which are used to distinguish one fluid from another. *Level Set Methods* (*LSM*) were introduced by Osher and Sethian [18] and rely on

* Corresponding author.
E-mail address: acharya@me.lsu.edu (S. Acharya).

0017-9310/$ - see front matter © 2008 Elsevier Ltd. All rights reserved.
doi:10.1016/j.ijheatmasstransfer.2007.11.055

Nomenclature

$\mathbf{b}_s$	specific body force at the material point (m/s^2)
$\mathbf{b}_{s,i}$	body force at the nodes of the background grid (N)
C_{ps}	pressure coefficient
c_1, c_2	constants in Mooney law
C_d	drag coefficient
$\mathbf{e}_\mathrm{g}$	gravity force-directed unit vector
$\mathbf{f}_\mathrm{i}^\mathrm{int}$	internal force at the nodes of the background grid (N)
$\mathbf{f}_\mathrm{i}^\mathrm{ext}$	external force at the nodes of the background grid (N)
g	specific gravitational force (m/s^2)
Gr	Grashof number
$G_i(\mathbf{r}_s)$	gradient of the shape function (1/m)
h_0	initial thickness of a shell (m)
L_0	characteristic length (m)
m_s	mass of material point (kg)
m_i	mass at the nodes of the background grid (kg)
$\mathbf{n}_\Gamma$	normal to the surface of the body
N_s	number of the material points
Nu	Nusselt number
p	fluid pressure (Pa)
$\mathbf{p}_i^\Gamma$	traction vector at the background grid (N)
$\mathbf{p}^\Gamma(\mathbf{r}_s, t)$	specific traction vector at the material point (N m/kg)
Pr	Prandtl number
r_0	initial radius (m)
$\mathbf{r}_s^n$	current position of the material points (m)
Re	Reynolds number
$S_i(\mathbf{r}_s^n)$	shape function
t^n	current numerical time step
T	fluid temperature (K)
T_0	characteristic temperature (K)
T^Γ	temperature of the immersed surface (K)
$\mathbf{u}_s$	displacement of the material point (m)
$\mathbf{v}^\Gamma$	velocity of the immersed surface (m/s)
$\mathbf{v}_s^n$	velocity of material point (m/s)
$\mathbf{v}_i$	velocity at the nodes of the background grid (m/s)
v_0	characteristic velocity (m/s)
$\mathbf{v}$	fluid velocity (m/s)
x_s	length of the bubble behind the sphere (m)

Greek symbols

α	thermal diffusivity (m^2/s)
β_T	coefficient of thermal expansion (1/K)
ε_s^n	strain of material point
ν	kinematic viscosity (m^2/s)
ρ_s^n	density of material point (kg/m^3)
$\boldsymbol{\sigma}_s$	Cauchy stress tensor (Pa)
$\boldsymbol{\sigma}_\mathrm{f}$	stress tensor of the fluid (Pa)
$\boldsymbol{\sigma}_s^n$	Cauchy stress tensor of material point (Pa)

an implicit formulation of the interface whose zero-level set always gives the location of the propagating interface through a solution of the time-dependent initial-value problem. These methods are attractive because they admit a convenient description of topologically complex interfaces and are quite simple to implement [19,20]. The *Fictitious Domain Method* (*FDM*) was introduced by Saul'ev [21] and has been primarily applied to the interaction of fluid with rigid body particles by Glowinski et al. [22,23]. The main idea of *FDM* consists of coupling of moving rigid particles with fluid by using a Lagrangian multiplier. A new method combining the fictitious domain [22] and the mortar element [24] methods for the computational analysis of fluid–structure interaction of a Newtonian fluid with slender bodies was developed by Baaijens [25]. An extension of this approach was used to describe the motion of a large leaflet and its interaction with the surrounding fluid [26].

The *Immersed Boundary Method* (*IBM*) was introduced by Peskin [27] to study the flow in a heart valve. The idea was very useful to solve *FSI* problems that included the free movement of a structure through a fluid domain. The interaction between the fluid and a deformable body was realized through nodal forces at selected grid points incorporated in the momentum equations. These external terms were spread over the computational domain through smoothed approximation of the Dirac delta function and satisfied the boundary conditions on the surface. This approach is associated with some disadvantages inherent to the diffuse-interface methods. For example, *IBM* is only first-order accurate in space and the boundary spreads over 3–5 grid nodes. A short review of Immersed Boundary and Cartesian Cut Methods for flows with moving boundaries was recently published by Mittal and Iaccarino [28].

The *Immersed Interface Method* (*IIM*) was designed by LeVeque and Li [29] to further develop the *IBM* of Peskin [30]. Instead of using a smooth approximation of the delta function, the *IIM* used approximations of the delta function with discontinuity across the boundary (jump conditions). Thus, the *IIM* is classified as a sharp-interface method. In [31,32] it was shown that *IIM* has second-order accuracy and is free from shortcomings of *IBM*. The *Immersed Finite Element Method* was developed by Zhang et al. [33] where the fluid and solid body are modeled with the finite element method. To avoid expensive grid regeneration, a fixed Eulerian grid for the fluid was used. The connection between the Lagrangian solid body and the fluid was implemented as in the *IBM*, but instead of the Dirac delta function, the higher-order reproducing kernel particle method (*RKPM*) [34] delta function was used.

A variant of the classical *IBM* [27] approach that does not require the explicit addition of discrete forces to the governing equations was developed by Mohd-Yusof [35] and Fadlun et al. [36]. This approach treats the solid boundary as a sharp interface. The specific values of various flow variables at the near-boundary nodes are calculated by interpolating linearly along an appropriate grid line between the nearest interior node, where flow variables are available from the solution of the governing equations, and the point where the grid line intersects the solid boundary, where physical boundary conditions are known. This approach can be classified as a *Hybrid Cartesian-Immersed Boundary* (*HCIB*) approach [36].

A new *HCIB* formulation applicable to three-dimensional flows with arbitrarily complex immersed boundaries moving with prescribed motion was developed in [37]. This methodology maintains a sharp fluid-body interface by discretizing the body surface using an unstructured, triangular mesh. The nodes of this mesh constitute a set of Lagrangian control points, which are used to track the motion and reconstruct the instantaneous shape of the moving immersed boundary. The reconstruction of the solution at the near-boundary nodes is carried out using interpolation along the normal to the body [38].

The most common strategy for solving structural deformation in problem involving fluid–structure interaction is the *finite element method (FEM)* [39]. In contrast to these studies, the *material point method* (*MPM*) [40] has certain advantage over standard *FEM* including the ability to handle large structural deformations. While the *MPM* has been demonstrated in a number of studies to be an effective strategy for solid objects, its use in resolving *FSI* is limited to that of York et al. [41] who utilized an *MPM* approach both the fluid and solid.

The purpose of this study is to develop a numerical method to simulate heat transfer problems for deformable bodies moving and interacting with the surrounding fluid. Our method combines *HCIB* method [37] to resolve the flow around a body with complex shape and *MPM* [41] to solve for the deformation of the solid structure moving under forces from the surrounding fluid. Instead of *HCIBM* which uses a Cartesian grid, we use the term *HIBM* to emphasize that we have realized this method in general curvilinear grid [42,43]. The method is validated by solving for sphere falling in a channel/box under the action of gravitational forces. The predicted data is in excellent agreement with experimental data of Cate et al. [44]. Because a full system of *HIBM* & *MPM* equations was solved (on the assumption that solid body has a high rigidity) this test validates *FSI* algorithm. For the validation of the heat transfer problem, a steady flow past a hot sphere was considered and predictions were compared with data of Bagchi et al. [45]. The calculated Nusselt numbers are in good agreement with the cited data. The *HIBM* & *MPM* approach was finally applied to a deforming sphere and the difference in heat transfer between a rigid and deforming sphere are presented and discussed.

The focus of this paper is to demonstrate the applicability of the *HIBM* and *MPM* strategy for *FSI* problems involving heat transfer. To our knowledge, this is the first application of such an approach for heat transfer problems.

2. Governing equations

The specific aim of the present paper is to develop and validate an efficient numerical method for simulating unsteady, three-dimensional flows and heat transfer for complex and deformable bodies. The unsteady, 3D, incompressible Navier–Stokes (NS) equations are solved using an efficient finite-difference method that is second-order accurate both in space and time. A hybrid approach that combines curvilinear grids, and the immersed boundary method was used to develop a powerful and very general methodology for efficiently and accurately resolving all geometrical features of flow. The deformations of the bodies are calculated as part of the solution procedure by implementing a fluid–structure interaction (*FSI*) model. The mathematical model consists of the momentum equations for the flow, the equations for the material velocity (deformation rate) for the solid body, the continuity and energy equations for the fluid, the continuity equation for the solid structure, and the appropriate boundary conditions.

Flow and heat transfer in the fluid region is described by the full 3D Navier–Stokes equations and the energy equations with the Boussinesq approximation as

$$\nabla \cdot \mathbf{v} = 0, \tag{1}$$

$$\frac{\partial \mathbf{v}}{\partial t} + (\mathbf{v}\cdot\nabla)\mathbf{v} + \nabla p = \frac{1}{Re}\Delta \mathbf{v} + \frac{Gr}{Re^2} T \mathbf{e}_g, \tag{2}$$

$$\frac{\partial T}{\partial t} + (\mathbf{v}\cdot\nabla)T = \frac{1}{RePr}\Delta T, \tag{3}$$

where $\mathbf{v}$ is the velocity, p is the pressure, T is the temperature, $\mathbf{e}_g$ is the gravity force-directed unit vector. These equations were normalized as

$$x = \frac{\tilde{x}}{L_0}, \quad v = \frac{\tilde{v}}{v_0}, \quad t = \frac{\tilde{t}}{t_0}, \quad p = \frac{\tilde{p}}{p_0}, \quad T = \frac{\widetilde{T} - \widetilde{T_0}}{\widetilde{T_w} - \widetilde{T_0}}$$

where the tilde denotes dimensional quantities, L_0 (m), v_0 (m/s), T_0 (K) are some characteristic length, velocity, and temperature.

The key non-dimensional numbers are

$$Re = \frac{v_0 L_0}{\nu}, \quad Pr = \frac{\nu}{\alpha}, \quad Gr = \frac{\beta_T (T^\Gamma - T_0) g L_0^3}{\nu^2}$$

where Re is the Reynolds number, Pr is the Prandtl number, Gr is the Grashof number, ν is the kinematic viscosity, α is the thermal diffusivity, β_T is the coefficient of thermal expansion, g is the specific gravitational force, T^Γ is the temperature of the immersed body.

The equations for the solid deformable body are given in an Eulerian frame because, as discussed later an Eulerian background grid is used to solve the solid body equations:

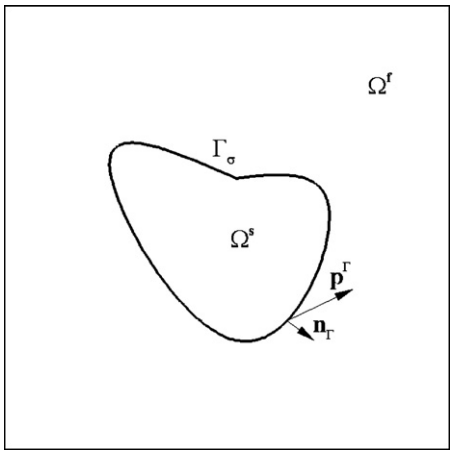

Fig. 1. Computational region for fluid Ω^f and immersed body Ω^s. Γ_σ is the boundary with imposed force from fluid.

$$\frac{d\rho_s}{dt} + \rho_s \nabla \cdot \mathbf{v}_s = 0, \tag{4}$$

$$\rho_s \frac{d\mathbf{v}_s}{dt} = \nabla \cdot \boldsymbol{\sigma}_s + \rho_s \mathbf{b}_s, \tag{5}$$

where $\mathbf{v}_s = d\mathbf{u}_s/dt$ is velocity, $\mathbf{u}_s$ is displacement, $\boldsymbol{\sigma}_s$ is the Cauchy stress tensor, $\mathbf{b}_s$ is the specific body force. Relations between the strain and the stress tensor given by the Mooney's law [46].

In order to get a numerical solution for a given *FSI* problem, boundary conditions must be specified for the above-mentioned systems of equations (see Fig. 1 for notations):

(a) boundary condition for fluid velocity $\mathbf{v}$ and temperature T are implemented on the immersed surface

$$\mathbf{v} = \mathbf{v}^\Gamma, \quad T = T^\Gamma, \quad \text{on } \Gamma_\sigma, \tag{6}$$

where $\mathbf{v}^\Gamma$ is velocity, T^Γ is the temperature of the immersed surface,

(b) boundary condition for the surface traction

$$\boldsymbol{\sigma}_f \cdot \mathbf{n}_\Gamma = \mathbf{p}^\Gamma, \quad \text{on } \Gamma_\sigma, \tag{7}$$

where $\boldsymbol{\sigma}_f$ is stress tensor of the fluid, $\mathbf{p}^\Gamma$ is the traction vector, $\mathbf{n}_\Gamma$ is the normal to the surface Γ.

3. Solution procedure

3.1. Solution of the fluid equations

The discrete equations are integrated in time via a second-order accurate dual time-stepping, artificial compressibility iteration scheme. To solve the system of governing equations (1)–(3), a pressure-based Residual Smoothing Operator, Multistage Pseudocompressibility Algorithm developed by Sotiropoulos and Constantinescu [47] was used. This approach incorporates the idea of combining pressure-based method [48] and the Artificial Compressibility [49] method to get an efficient diagonal pressure-based operator which was implemented in a four-stage Runga–Kutta algorithm. Sotiropoulos and Constantinescu [47] have shown that this algorithm substantially enhances the damping of high-frequency errors on large aspect ratio meshes. Since details of this algorithm are available in earlier papers [47–49], additional details are not given here.

3.2. Solution of the solid equations

The Material Point Method (*MPM*) [40,41,50,51] is used for solving the governing equations for the solid structure (Eq. (4) and (5)). The common approach for solving solid mechanic problems is the finite element method (*FEM*), but as noted earlier, in problems with large material deformations, the mesh can get quite distorted, and in such case can lead to loss of accuracy. The *MPM* is a meshless method that is conceptually derived from the particle in cell method of Harlow [52], and was developed to accommodate large distortions. This property of *MPM* is clearly an advantage in comparison with the *FEM*.

We will briefly describe the algorithm of *MPM*. The solid domain is covered with an arbitrary number of material points. Let $\mathbf{r}_s^n, s = 1, \ldots N_s$ denote the current position of the material points at time t^n, N_s is the number of the material points. Each material point has an associated mass, m_s, density, ρ_s^n, velocity, $\mathbf{v}_s^n$, Cauchy stress tensor, $\boldsymbol{\sigma}_s^n$, and strain, ε_s^n at time t^n. In the present *HIBM* & *MPM* we obtain the solution of the solid equations on a Cartesian background grid which is independent from the fluid grid. The momentum equations (5) are interpolated to the Cartesian background grid i by means of shape functions $S_i(\mathbf{r}_s^n)$ similar to those used in a standard *FEM* techniques to get the system of algebraic equations. In all the notations we will use here, the subscript s will denote material points and the subscript i (j) will represent the background grid nodes. The momentum equation (5) on the background grid (weak form) is given by [41]

$$m_i \frac{d\mathbf{v}_i}{dt} = \mathbf{f}_i^{\text{int}} + \mathbf{f}_i^{\text{ext}}, \tag{8}$$

where $\mathbf{f}_i^{\text{int}}$ is the internal force, $\mathbf{f}_i^{\text{ext}}$ is the external force, $m_i = \sum_{s=1}^{N_s} m_s S_i(\mathbf{r}_s)$ is the mass, $\mathbf{v}_i = \sum_{s=1}^{N_s} \mathbf{v}_s S_i(\mathbf{r}_s)$ is the velocity on the background grid. Internal and external forces are given by

$$\mathbf{f}_i^{\text{int}} = -\sum_{s=1}^{N_s} (m_s/\rho_s) \boldsymbol{\sigma}_s \cdot G_i(\mathbf{r}_s), \tag{9}$$

$$\mathbf{f}_i^{\text{ext}} = \mathbf{p}_i^{\Gamma,t} + \mathbf{b}_{s,i}, \tag{10}$$

where $G_i(\mathbf{r}_s) = \mathbf{V} S_i|_{\mathbf{r}_s} = [\partial S_i/\partial x, \partial S_i/\partial y, \partial S_i/\partial z]^{\mathrm{T}}_{\mathbf{r}_s}$, is the gradient of the shape functions, and the discrete specific traction vector on the background grid is

$$\mathbf{p}_i^\Gamma = \sum_{s=1}^{N_s} m_s \mathbf{p}^\Gamma(\mathbf{r}_s, t) S_i(\mathbf{r}_s) h^{-1}(\mathbf{r}_s, t), \tag{11}$$

where $\mathbf{p}^{\Gamma}(\mathbf{r}_s,t)$ is a specific traction vector at the material points on the surface of the solid body (i.e., traction divided by mass density), $h^{-1}(\mathbf{r}_s,t)$ is the thickness of a shell or membrane (only such objects are considered in this paper). The body force is represented as

$$\mathbf{b}_{s,i} = \sum_{s=1}^{N_s} m_s \mathbf{b}_s(\mathbf{r}_s,t) S_i(\mathbf{r}_s). \tag{12}$$

Eqs. (8)–(12) are solved by using an explicit finite-difference scheme [41].

3.3. Fluid–structure interaction algorithm

At every instant in time, the influence of the body on the flow is accounted for by applying boundary conditions at grid nodes located in the immediate vicinity of the body. The immersed boundary is treated as a sharp interface and the solution in its vicinity is reconstructed using interpolation along the local normal to the body [38]. Boundary conditions from the fluid on the solid immersed body define its motion. The complete fluid–structure interaction algorithm is implemented by solving Eqs. (1)–(7). At every time step we solve the Navier–Stokes equations (1)–(3) for the known geometry of the immersed body and boundary conditions at the immersed boundary nodes (6). Next, we define the boundary conditions (7) on the solid surface represented by fluid stresses acting on the body. Under the influence of boundary stresses or forces, the body is deformed according to Eqs. (4) and (5). New coordinates of the immersed body and boundary conditions at immersed boundary nodes for fluid (6) are established which are used for the solution of the Navier–Stokes equations at the next time step.

4. Validation tests

The goal of the present paper is to validate the combined *HIBM & MPM* as a strategy for solving *FSI* problems with strong structural deflections and heat transfer between the deformable body and fluid. In this section we will present several validation studies and compare with available data/theory/published simulations to demonstrate the accuracy of the approach.

4.1. Inflating elastic sphere

As a first step to verify the *MPM*, we have solved the problem of an inflating spherical elastic shell under the action of internal pressure. For Mooney's material an analytical solution that provides the relation between the radial deformations λ_1 and the pressure p is known [46]

$$p = \frac{8h_0}{r_0\lambda_1}(1-\lambda_1^{-6})(c_1+c_2\lambda_1^2), \tag{13}$$

where r_0 is the initial radius, $h_0 = 0.02r_0$ is the initial thickness of a shell, and $c_1 = 20$ and $c_2 = 10$ represent of the Mooney material given by the equation for the stress T_1 acting on the membrane [46]

$$T_1 = 4h_0(1-\lambda_1^{-6})(c_1+c_2\lambda_1^2).$$

Table 1
Inflating elastic sphere: comparison of calculated strain-pressure dependence with analytical solution [46]

$r_0p/8h_0c_1$	λ_1 350 Δ elements	λ_1 1026 Δ elements	λ_1 3782 Δ elements	Analytical solution [46]
0.55	1.05	1.08	1.08	1.082
0.94	1.12	1.15	1.16	1.19
1.24	1.25	1.32	1.35	1.42
1.54	1.71	1.92	2.11	2.19
1.87	2.52	2.81	3.01	3.11
2.45	3.82	4.08	4.41	4.45

The sphere surface was discretized with 350, 1026, and 3782 triangular elements and solutions for three meshes are shown in Table 1. In order to get the needed stationary solution we have used a quasi-stationary approach. The pressure inside the sphere was increased incrementally and at each value of the internal pressure the steady solution was found. As seen in Table 1 the agreement of our numerical solution with the analytical solution is good with a maximum deviations of less that 5%.

4.2. Sphere falling in a box under gravity

To validate the *HIBM & MPM* algorithm we solved a problem of a sphere falling in a channel (with a closed bottom) under the action of gravitational forces. We compared the data from experiment of Cate et al. [44] with the present numerical simulation obtained by the solution of the coupled system of fluid and solid equations. The complete *HIBM & MPM* algorithm was implemented and tested. Cate et al. [44] performed experimental and computational studies of nylon sphere with a diameter $d = 0.015$ m and density $\rho_s = 1120\ \mathrm{kg/m^3}$ falling in a box with size of $0.1 \times 0.1 \times 0.16\ \mathrm{m^3}$ under the action of gravitational force. The initial position of the particle was at a

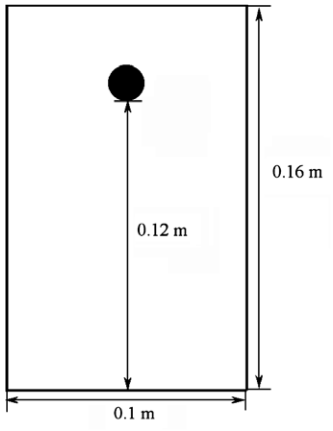

Fig. 2. Picture of a box used in experiment of [44].

Table 2
Fluid properties in the experiments of Cate et al. [44]

# Experiment	ρ_f (kg/m^3)	μ_f (10^{-3} Pa s)	u_∞ (m/s)	Re
1	962	113	0.091	11.6
2	960	58	0.128	31.9

height $h = 0.12$ m from the bottom of the box (Fig. 2). As the particle is rigid, in the *FSI* algorithm we used high rigidity of the material of the sphere represented by $c_1 = 10^5, c_2 = 10^5$, where c_1, c_2 are constants describing the properties of Mooney's material [46].

Table 2 shows the property data of two experiments used in our simulations at two Reynolds numbers, $Re = 11.6$ and 31.9. The Reynolds number was defined on the basis of the terminal velocity of the particle as given by Abraham [53].

To discretize the computational region we used three grids to show the accuracy and convergence of computational data: (I) – $25 \times 25 \times 40$, (II) – $50 \times 50 \times 80$, and (III) – $100 \times 100 \times 160$ grid nodes. For all grids, a physical time step of $\Delta t = 10^{-2}$ was used. The sphere surface was discretized with 350/177, 1026/515 and 3782/1893 triangular elements/nodes respectively for the three different sets of grid (I), (II), and (III). In accordance with the experiments, non-slip boundary conditions were utilized at all walls of the box and non-reflecting boundary conditions [54] was implemented on the top boundary.

Fig. 3 shows the time history of velocities of the particle falling in the box for (a) $Re = 11.6$, and (b) $Re = 31.9$. Data are presented for three types of grids (I)–(III) and it is evident that the finest grid solution convergence to the experimental data for both cases. As is seen from Fig. 3, the particle experiences an initial acceleration, followed by steady fall and deceleration near the bottom of the box, due to influence of the lower solid boundary. We do not use any special strategy for simulating the force on the particle when it approaches the bottom of the box [44,55], and because of this, the predictions for settling velocities are shown only up to the time instances when particles begin to decelerate. We note that the deceleration of particles depends on the grid and begins earlier for the coarser grid. For the finest grid $100 \times 100 \times 160$ comparison of experimental and computed data shows good agreement.

Fig. 4 shows the time history of the drag coefficient for $Re = 11.2$ and $Re = 31.9$ in the time interval $0s \leqslant t \leqslant 1s$. Eq. (14) provides the expression for the steady drag coefficient given by Abraham [53]

$$C_d = \frac{24}{9.06^2}\left(\frac{9.06}{\sqrt{Re}} + 1\right)^2. \tag{14}$$

The steady values of C_d predicted for both Reynolds numbers are close to Eq. (14), as shown in Fig. 4, and the difference between them is less than 10%.

The pressure contours and velocity streamlines are shown in Fig. 5 at three different time instances during the descent of the particle for $Re = 11.6$. The sphere is seen

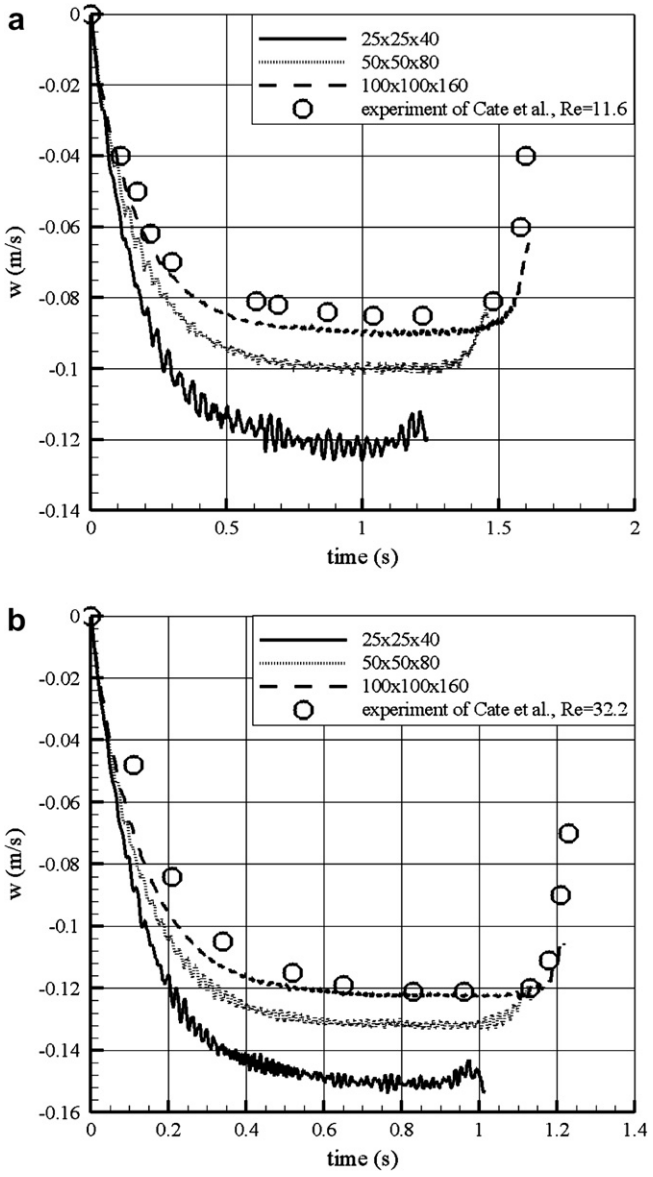

Fig. 3. Simulation of falling a sphere in a tube. (a) $Re = 11.6$. (b) $Re = 31.9$. Three types of grid were used, solid (I) $25 \times 25 \times 40$, dotted (II) $50 \times 50 \times 80$, and dashed (III) $100 \times 100 \times 160$. Experimental data [44] shown in open circle.

to retain its originally spherical shape at each time step indicating that the structural calculations are correctly predicting negligible deformations of the rigid shell. The flow field appears to predict the correct qualitative features with the flow symmetry across the channel centerline, separation near $\theta = 90^0$, and higher pressures at the stagnation leading edge of the sphere.

4.3. Validation of heat transfer. Flow past a hot rigid sphere

To validate *HIBM & MPM* method for heat transfer problems, flow past a hot rigid sphere was studied for the steady case and compared with the direct simulation results in [45].

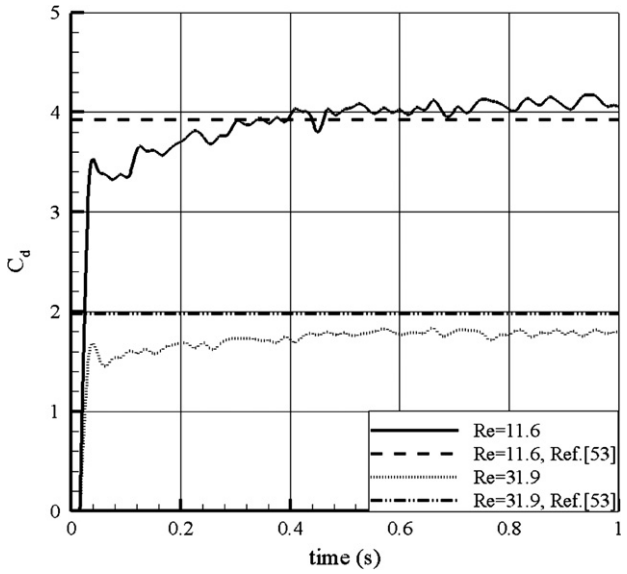

Fig. 4. Time history of the drag coefficient C_d for two Reynolds numbers: solid line is $Re = 11.6$, dashed line is $Re = 31.9$. Exact solutions are data from [53].

The simulations were performed for Reynolds number $Re = 50$, 100, and 200. Flow past a fixed sphere, in the form of streamlines, are shown in Fig. 6 for $Re = 100$. The size of grid in vicinity of the sphere is $h = 0.025$, and the corresponding length of the bubble behind the sphere is $x_s = 0.86$. This represents a discrepancy of less than that 5% from the solution in [56].

For a quantitative assessment of a heat transfer from the sphere, the dimensionless local heat transfer coefficient or the Nusselt number is defined as

$$Nu = \nabla T \cdot \mathbf{n}_s,$$

where $\mathbf{n}_s$ is a normal vector to the surface of the sphere. Fig. 7 shows a variation of Nusselt numbers for $Re = 50$, 100, and 200 for grids $h = 0.05$, and $h = 0.025$. In our case $\theta/\pi = 0$ corresponds to the front stagnation point and $\theta/\pi = 1$ is the rear stagnation point of the body. Our predictions show good agreement with [45] for the finest grid $h = 0.025$, with the differences being less than 5%. This confirms that a grid size $h = 0.025$ can be used for simulation of heat transfer problems for Reynolds numbers $Re = 50$ to $Re = 200$.

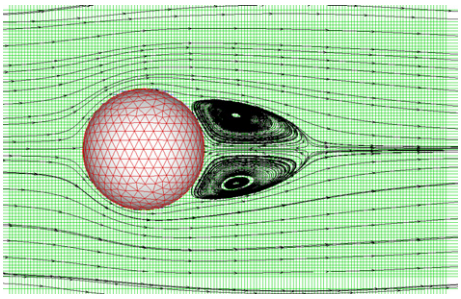

Fig. 6. Simulation of flow past a sphere. Streamlines and stretched grid in the vicinity of the sphere for $Re = 100$.

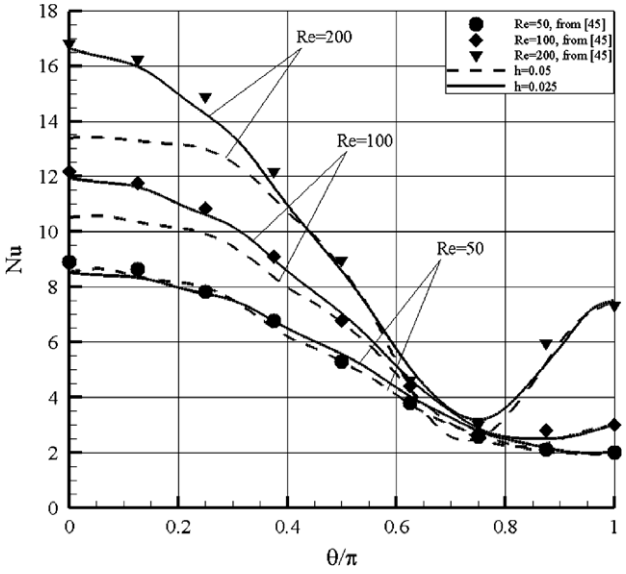

Fig. 7. Simulation of flow past a sphere. Variation of Nusselt number for flow past a sphere for $Re = 50, 100, 200$. Solid lines are $h = 0.05$, dashed lines are $h = 0.025$. Circles, diamonds, and gradients are data from Bagchi et al. [45].

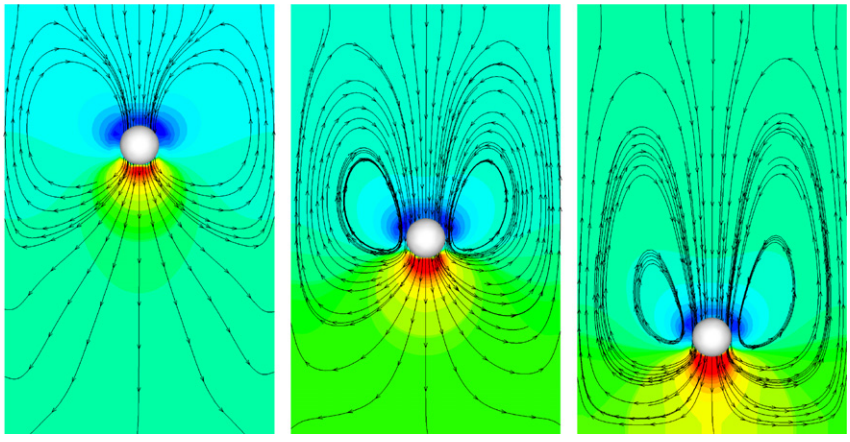

Fig. 5. Simulation of falling rigid sphere in a tube. $Re = 11.6$. Contours of pressure and streamlines, $t_1 = 0.4$ s, $t_2 = 0.8$ s, $t_3 = 1.2$ s.

5. Heat transfer from a solid and deformable sphere

As a final example involving heat transfer, we consider a hot deformable sphere falling in a channel under the action of a gravitational force. A number of practical examples that involve moving hot spheres include spray cooling, plasma sprays, quenching of ball bearings, etc. For simplicity, we consider here the case of an isothermal sphere, and examine the Nusselt number around the sphere with deformations. While we have considered isothermal sphere in this paper, conjugate heat transfer aspects that include the solution of heat conduction equation inside the sphere can easily be incorporated.

Calculations were carried out for a Reynolds number $Re = 50, 100$ and Prandtl number $Pr = 0.72$ on the uniform grid with $81 \times 81 \times 241$ nodes ($h = 0.05$). The sphere surface was discretized with 1026 triangular elements. The initial non-dimensional temperature for the fluid is $T_0 = 0$, the temperature of the sphere is held constant at $T^{\Gamma} = 1$. On the top, bottom and on the sides of computational region non-reflecting boundary conditions for velocity and pressure, and $\partial T/\partial n = 0$ for temperature are used.

Fig. 8 shows the streamlines and temperature contours for the rigid and soft sphere (with material properties: $c_1 = 20$, $c_2 = 10$) in stationary coordinate system. The deformable body has moved further downstream compared to the rigid sphere. This is due to an initial decrease of the drag forces during the early-descent period. While the general flow distribution around both rigid and soft sphere are similar, there are noticeable differences when examined in a moving coordinate system (Fig. 9).

Fig. 9 shows the streamlines and temperature contours for steady flow past a rigid sphere (Fig. 9a), and b corresponding plots for the falling sphere (both rigid, Fig. 9b

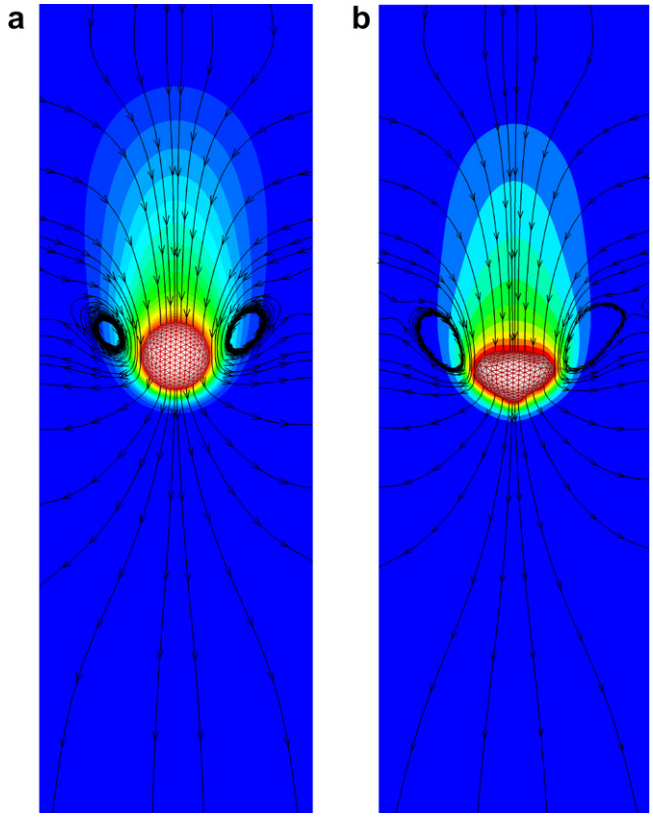

Fig. 8. Streamlines superposed on temperature contours for falling (a) rigid and (b) soft spheres, $Re = 50$. Stationary coordinate system. In Figs. 9–13, the parameters $c_1 = 20$, $c_2 = 10$ are used for the soft sphere.

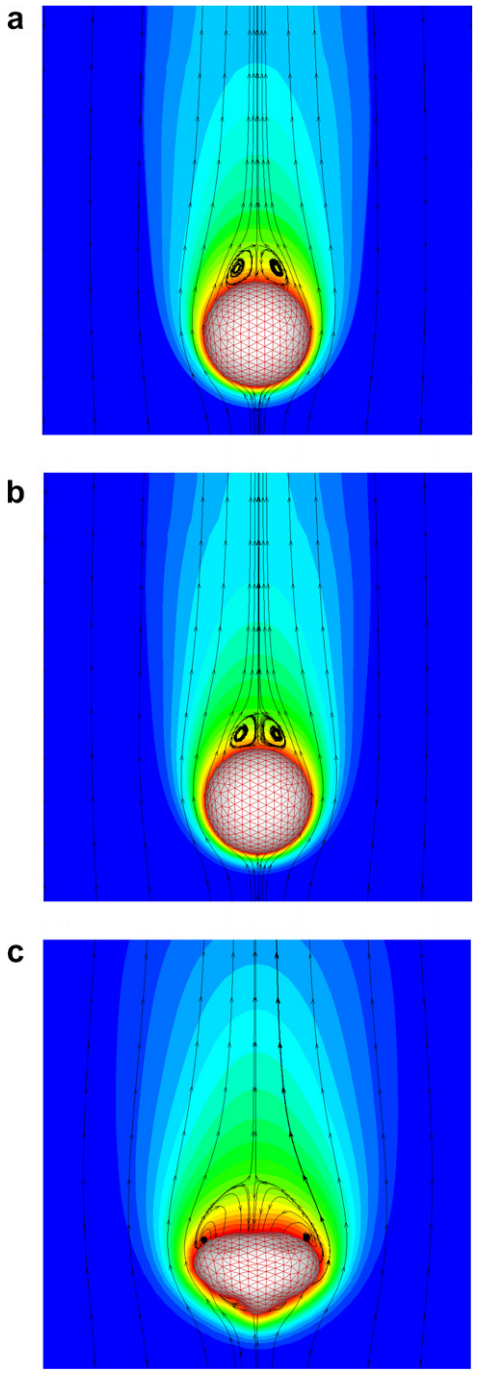

Fig. 9. Streamlines superposed on temperature contours for (a) steady flow past a rigid sphere, (b) falling rigid sphere, and (c) falling soft sphere. In (b) and (c) the mean velocity of the sphere is subtracted from the flow field to enable comparison with (a). $Re = 50$.

and deforming, Fig. 9c) at a given instance in time with the mean velocity of the moving sphere subtracted from the velocity field (coordinate frame fixed to the sphere so that relevant comparisons can be made with Fig. 9a). It can be clearly seen that the deformation of the sphere leads to a large separated wake region (Fig. 9c) relative to the rigid sphere (Fig. 9b). A careful examination of the temperature contours also indicates that higher temperatures (lower Nusselt numbers) are seen in the wake region of the deformed sphere.

Fig. 10 shows the temperature contours and velocity vectors at three different time instances $t_1 = 0.1$, $t_2 = 9.0$, and $t_3 = 18.0$ during the motion of the soft sphere. It can be seen that the body is deformed progressively under the action of fluid stresses. The deformed sphere has a pear-shape with a larger cross-section at the top and a narrowing towards the front. As the body deforms the flow separation near $\theta/\pi = 0.5$ appears to be influenced, becoming progressively smaller.

Fig. 11 shows variations of Nusselt number along the surface of the deformable body at three instants of time $t_1 = 0.1$, $t_2 = 9.0$, and $t_3 = 18.0$ (see Fig. 10) during the descent of the body for $Re = 50$. For the falling rigid sphere, the Nu distribution approaches the steady-rigid sphere distribution with increasing time. The peak Nu occurs at the stagnation point $\theta/\pi = 0$, while the minimum Nu occurs at $\theta/\pi = 1$ in all these cases. However, for the deforming sphere, the distribution looks substantially different. The Nu values are generally lower, and the distributions exhibit significant non-uniformity with θ/π. The Nu minimum, at later instances in time, occurs in the range of $0.5 < \theta/\pi < 0.8$ instead of $\theta/\pi = 1$ for the rigid cases. Only Nu_{max} in front of body and a local Nu_{min} on the back side of the body are close to the Nu number for rigid sphere. Global Nu_{min} is close to point on the body with maximum curvature.

Fig. 12 shows the variations of Nusselt number along the surface of the deformable body at three instants of time during the descent of the body for $Re = 100$. In this case as well as for $Re = 50$, heat transfer (Nu) is less than in case of steady flow around a rigid sphere. The leading edge Nusselt number are clearly lower for the deforming sphere compared to the rigid sphere, and the minimum in Nu occurs at an earlier θ/π.

Pressure coefficient $C_{ps} = (p - p_\infty)/0.5\rho v_0^2$ on the surface of the deforming body at different instants of time is shown on Fig. 13 for $Re = 100$. In comparison with steady flow around the rigid sphere (solid line) and the falling rigid sphere (lines with dark circles) one can see a difference in the pressure distribution between the deformable and the rigid body. These differences are significant at time t_1 but with the increasing time the pressure coefficient approaches the rigid sphere value. It can seen that for the deforming sphere there is a reduction in the pressure on the back side

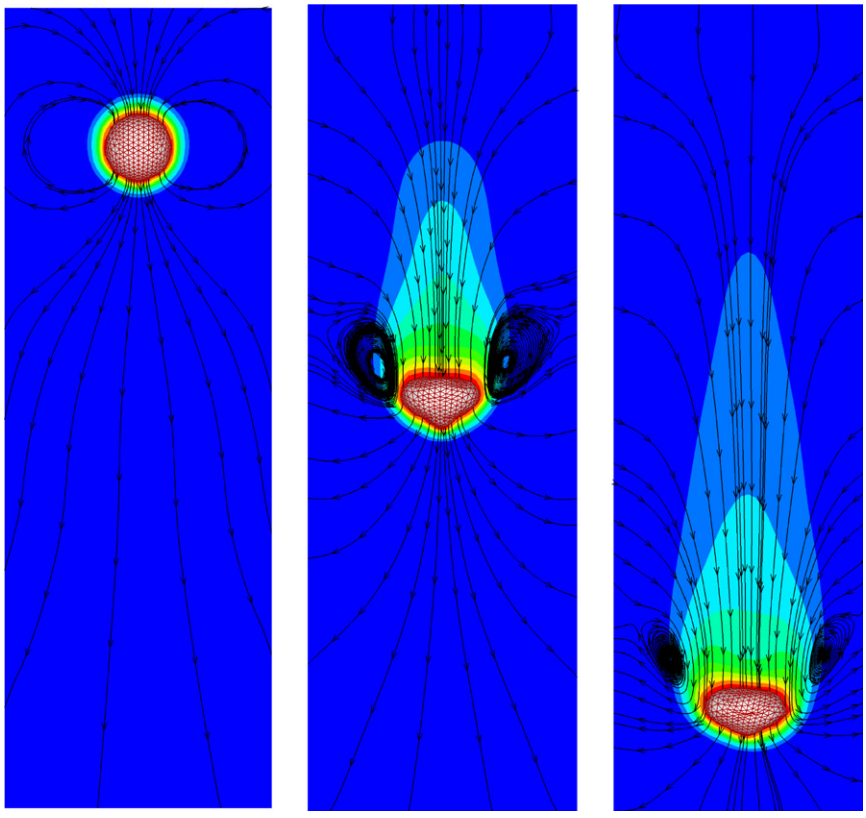

Fig. 10. Instantaneous streamlines and temperature contours at the $y =$ constant mid-plane at three time instances $t_1 = 0.1$, $t_2 = 9.0$, and $t_3 = 18.0$ around a falling soft hot sphere in the channel for $Re = 100$. Temperature levels are changed from $T_0 = 0$ to $T_w = 1.0$ with step $\Delta T = 0.05$.

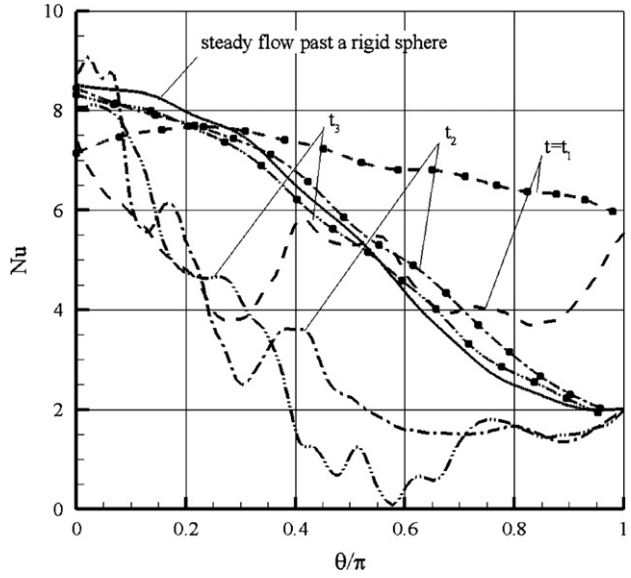

Fig. 11. Variation of Nusselt number for $Re = 50$ for rigid and deformable spheres ($c_1 = 20, c_2 = 10$). Time levels t_1, t_2, and t_3 are same as in Fig. 10. Solid line is Nu for flow past a rigid sphere ($h = 0.025$), dashed lines are Nu for rigid and soft sphere for t_1, dash-dot lines are Nu for t_2, and dash-dot-dot lines are Nu for t_3. Lines for falling rigid sphere are marked with dark circles.

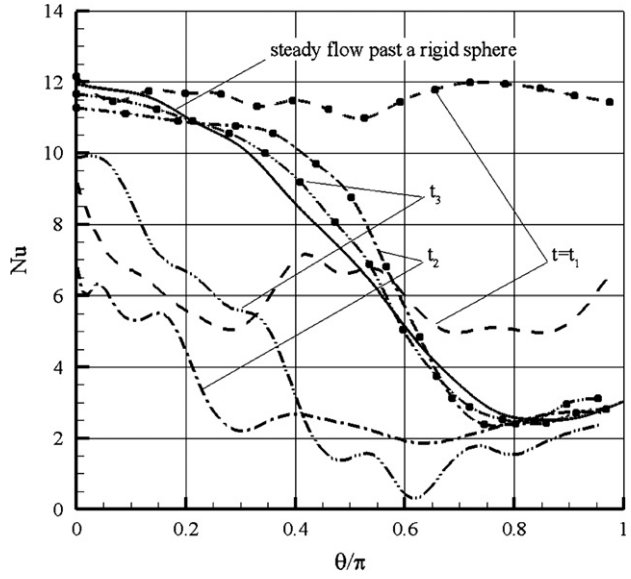

Fig. 12. Variation of Nusselt number for $Re = 100$ for rigid and deformable spheres. Legend – see Fig. 11.

of the body in comparison with the rigid sphere. This indicates an increase in the drag force for the deforming sphere. For $Re = 50$ the drag coefficient for soft sphere is approximately 1.3 times greater than that for the rigid sphere and is equal to $C_d = 2.2$. Our calculations give the drag coefficient for rigid sphere $C_d = 1.65$ that differs by about 5% from the known value $C_d = 1.57$ [45].

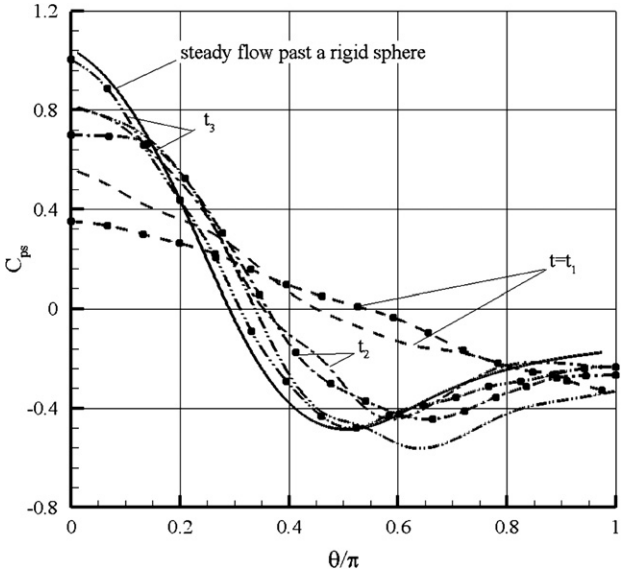

Fig. 13. Variation of pressure coefficient C_{ps} for $Re = 100$ for rigid and deformable spheres. Legend – see Fig. 11.

6. Concluding remarks

A numerical method for simulating *Fluid–Structure Interaction* problems with heat transfer has been presented. The method developed uses the *Immersed Boundary Method* for resolving complex boundaries for the fluid flow, and couples this with the *Material Point Method* for the structural stresses and deformation. The methodology is ideally suited for flow problems with initially complex geometries where the surfaces undergo large structural deformation. The methodology is demonstrated on a number of simple test cases including those involving heat transfer and show reasonable qualitative and quantitative agreement with published results.

Simulations of flow and heat transfer around a deforming hot sphere show that the sphere deforms in an inverted pean shape and Nusselt number distributions for deforming sphere have lower magnitudes relative to a solid rigid sphere. The location of minimum Nu is shifted to a lower θ/π value for the deforming sphere in view of the altered flow structure. Pressure distributions for the rigid and deformable sphere also differ from each other.

Acknowledgements

This work was supported by a Health Excellence Grant to the Biological Computation and Visualization Center (BCVC) by the State of Louisiana. Their support is greatly appreciated.

References

[1] R. Scardovelli, S. Zaleski, Direct numerical simulation of free-surface and interfacial flow, Ann. Rev. Fluid Mech. 31 (1999) 567–603.

[2] S. Popinet, S. Zaleski, A front-tracking algorithm for accurate representation of surface tension, Int. J. Numer. Methods Fluids 30 (1999) 775–793.
[3] M. Fritts, 3-Dimensional algorithm for grid restructuring in free Lagrangian calculations, Lecture Notes in Physics, vol. 238, New York, Springer-Verlag, 1985, pp. 122–144.
[4] C.W. Hirt, A.A. Amsden, J.L. Cook, An arbitrary Lagrangian–Eulerian computing method for all flow speeds, J. Comput. Phys. 14 (3) (1974) 227–253.
[5] J. Donea, S. Giuliani, J. Halleux, An arbitrary Lagrangian–Eulerian finite element method for transient dynamic fluid–structure interactions, Comput. Methods Appl. Mech. Eng. 33 (1982) 689–723.
[6] T. Belytschko, J. Kennedy, Finite element approach to pressure wave attenuation by reactor fuel subassemblies, J. Press. Technol. (1975) 172–177.
[7] J. Donea, P. Fasoli-Stella, S. Giuliani, Finite element solution of transient fluid–structure problems in Lagrangian coordinates, in: Proceedings of the International Meeting on Fast Reactor Safety and Related Physics, Chicago, vol. 3, 1976, pp. 1427–1435.
[8] H. Liu, K. Kawachi, A numerical study of undulatory swimming, J. Comput. Phys. 155 (2) (1999) 223–247.
[9] W. Noh, CEL: A time-dependent, two-space-dimensional, in: Coupled Eulerian–Lagrange Code, Methods in Computational Physics, Academic Press, New York, 1964, pp. 117–179.
[10] H. Udaykumar, H.-C. Kan, W. Shyy, R. Tran-Son-Tay, Multiphase dynamics in arbitrary geometries on fixed Cartesian grids, J. Comput. Phys. 137 (1997) 366–405.
[11] A.S. Almgren, J.B. Bell, P. Colella, T. Marthaler, A Cartesian grid projection method for the incompressible Euler equations in complex geometries, SIAM J. Sci. Comput. 18 (5) (1997) 1289–1309.
[12] H. Johansen, P. Colella, A Cartesian grid embedded boundary method for Poisson's equation on irregular domains, J. Comput. Phys. 147 (1998) 60–85.
[13] H.S. Udaykumar, R. Mittal, P. Rampunggoon, A. Khanna, Sharp interface Cartesian grid method for simulating flows with complex moving boundaries, J. Comput. Phys. 174 (2001) 345–380.
[14] S. Popinet, Gerris: a tree-based adaptive solver for the incompressible Euler equations in complex geometries, J. Comput. Phys. 190 (2) (2003) 572–600.
[15] M. Kirkpatrick, S. Armfield, J. Kent, A representation of curved boundaries for the solution of the Navier–Stokes equations on a staggered three-dimensional Cartesian grid, J. Comput. Phys. 184 (1) (2003) 1–36.
[16] C. Hirt, B. Nichols, Volume of fluid (VOF) methods for the dynamics of free boundaries, J. Comput. Phys. 39 (1981) 201–225.
[17] J. Hyman, Numerical methods for tracking interfaces, Phys. D 12 (1984) 396–407.
[18] S. Osher, J. Sethian, Front propagating with curvature depend speed: algorithm based on Hamilton–Jacobi equations, J. Comput. Phys. 79 (1988) 12–49.
[19] J. Sethian, P. Smereka, Level set method for fluid interface, Ann. Rev. Fluid Mech. 35 (2003) 341–372.
[20] D. Enright, R. Fedkiw, J. Ferziger, I. Mitchel, A hybrid particle level set method for improved interface capturing, J. Comput. Phys. 183 (1) (2002) 83–116.
[21] V. Saul'ev, On the solution of some boundary value problems on high performance computers by fictitious domain method, Siberian Math. J. 4 (4) (1963) 912–925 (in Russian).
[22] R. Glowinski, T.-W. Pan, T.I. Hesla, D.D. Joseph, J. Periaux, A fictitious domain method with distributed Lagrange multipliers for the numerical simulation of particulate flow, Contemp. Math. 218 (1998) 121–137.
[23] R. Glowinski, T. Pan, T.I. Hesla, D.D. Joseph, J. Periaux, A fictitious domain approach to the direct numerical simulation of incompressible viscous flow past moving rigid bodies: application to particulate flow, J. Comput. Phys. 169 (2001) 363–426.
[24] C. Bernardi, Y. Maday, A. Patera, Domain decomposition by the mortar element method, in: H.G. Kaper, M. Garbey (Eds.), Asymptotic and Numerical Methods for PDEs with Critical Parameters. NATO ASI Series C: Mathematical and Physical Sciences, vol. 384, 1993, pp. 169–186.
[25] F. Baaijens, A fictious domain/mortar element method for fluid–structure interaction, Int. J. Numer. Methods Fluid 35 (2001) 743–761.
[26] J.D. Hart, G. Peters, P. Schreurs, F. Baaijens, A three-dimensional computational analysis of fluid–structure interaction in the aortic valve, J. Biomech. 36 (2003) 103–112.
[27] C. Peskin, Flow patterns around heart valves: a numerical method, J. Comput. Phys. 10 (1972) 252–271.
[28] R. Mittal, G. Iaccarino, Immersed boundary method, Ann. Rev. Fluid Mech. 37 (2005) 239–261.
[29] R.J. LeVeque, Z. Li, The immersed interface method for elliptic equations with discontinuous coefficients and singular sources, SIAM J. Numer. Anal. 31 (1994) 1019–1044.
[30] C. Peskin, Numerical analysis of blood flow in the heart, J. Comput. Phys. 25 (1977) 220–252.
[31] L. Lee, R.J. LeVeque, An immersed interface method for incompressible Navier–Stokes equations, SIAM J. Sci. Comput. 25 (3) (2003) 832–856.
[32] S. Xu, Z.J. Wang, An immersed interface method for simulating the interaction of a fluid with moving boundaries, J. Comput. Phys. 216 (2) (2006) 454–493.
[33] L. Zhang, A. Gerstenberg, X. Wang, W.K. Liu, Immersed finite element method, Comp. Methods Appl. Mech. Eng. 193 (2004) 2051–2067.
[34] W. Liu, S. Jun, Y. Zhang, Reproducing kernel particle methods, Int. J. Numer. Methods Fluids 20 (1995) 1081–1106.
[35] J. Mohd-Yusof, Combined Immersed Boundaries/B-Splines Methods for Simulations of Flows in Complex Geometries, CTR Annual Research Briefs, Stanford University, NASA Ames, 1997.
[36] E. Fadlun, R. Verzicco, P. Orlandi, J. Mohd-Yusof, Combined immersed-boundary finite-difference methods for three-dimensional complex flow simulations, J. Comput. Phys. 161 (2000) 35–60.
[37] A. Gilmanov, F. Sotiropoulos, A hybrid Cartesian/immersed boundary method for simulating flows with 3d geometrically complex moving bodies, J. Comput. Phys. 207 (2005) 457–492.
[38] A. Gilmanov, F. Sotiropoulos, E. Balaras, A general reconstruction algorithm for simulating flows with complex 3D immersed boundaries on Cartesian grids, J. Comput. Phys. 191 (2003) 660–669.
[39] T.E. Tezduyar, S. Sathe, K. Stein, Solution techniques for the fully discretized equations in computation of fluid–structure interactions with the space–time formulations, Comput. Methods Appl. Mech. Eng. 195 (2006) 5743–5753.
[40] H. Schreyer, D. Sulsky, S.-J. Zhou, Modeling delamination as a strong discontinuity with the Material Point Method, Int. J. Numer. Methods Eng. 191 (2002) 2483–2507.
[41] A.R. York II, D. Sulsky, H. Schreyer, Fluid–membrane interaction based on the Material Point Method, Int. J. Numer. Methods Eng. 48 (2000) 901–924.
[42] A. Gilmanov, S. Acharya, A fluid/structure interaction method for compliant biological tissues: application to simulate iris accommodation, in: 7th World Congress on Computational Mechanics, Los Angeles, 2006.
[43] A. Gilmanov, S. Acharya, An immersed boundary and material point methodologies for moving/compliant surfaces with heat transfer, in: Proceedings of ASME International Mechanical Congress and Exposition, Chicago, Illinois, 2006.
[44] A.T. Cate, C. Nieuwstad, J. Derksen, H. Van den Akken, Particle imaging velocimetry experiments and lattice-Boltzmann simulation on a single sphere setting under gravity, Phys. Fluids 14 (2002) 4012–4025.
[45] P. Bagchi, M. Ha, S. Balachandar, Direct numerical simulation of flow and heat transfer from a sphere in a uniform cross-flow, J. Fluid Eng. 123 (2001) 347–358.
[46] A. Green, J. Adkins, Large elastic deformation and non-linear continuum mechanics, Oxford, 1960.

[47] F. Sotiropoulos, G. Constantinescu, Pressure-based residual smoothing operators for multistage pseudo-compressibility algorithms, J. Comput. Phys. 133 (1) (1997) 129–145.
[48] F. Sotiropoulos, S. Abdallah, A primitive variable method for the solution of external, 3-D incompressible, viscous flows, J. Comput. Phys. 103 (2) (1992) 336–349.
[49] C. Merkle, M. Athavale, Time-accurate unsteady incompressible flow algorithm based on artificial compressibility, AIAA Paper 87-1137.
[50] Z. Chen, R. Brannon, An evaluation of the material point method, Tech. Rep. 2002-0482, SAND REPORT, Sandia National Laboratory, 2002.
[51] J. Guilkey, J. Weiss, Implicit time integration for material point method: quantitative and algorithmic comparison with the finite element method, Int. J. Numer. Methods Eng. 57 (2003) 1323–1338.
[52] F. Harlow, The particle-in-cell computing method for fluid dynamics, in: Methods in Computational Physics, Academic Press, New York, 1964, pp. 319–343.
[53] F. Abraham, Functional dependence of drag coefficient of a sphere on Reynolds number, Phys. Fluids 13 (1970) 2194.
[54] K.W. Thompson, Time-dependent boundary conditions for hyperbolic systems II, J. Comput. Phys. 89 (2) (1990) 439–461.
[55] A. Ladd, Sedimentation of homogeneous suspensions of non-Brownian spheres, Phys. Fluids 9 (1997) 491–499.
[56] T. Johnson, V.C. Patel, Flow past a sphere up to a Reynolds number of 300, J. Fluid Mech. 378 (10) (1999) 19–70.